Supporting Information

Unconventional Direct Synthesis of Ni₃N/Ni with N-Vacancies for Efficient and Stable Hydrogen Evolution

Doudou Zhang, Haobo Li,* Asim Riaz, Astha Sharma, Wensheng Liang, Yuan Wang, Hongjun Chen, Kaushal Vora, Di Yan, Zhen Su, Antonio Tricoli, Chuan Zhao, Fiona J. Beck, Karsten Reuter, Kylie Catchpole,* and Siva Karuturi*

Dr. Doudou Zhang, Ms. Astha Sharma, Dr. Wensheng Liang, Dr Fiona J. Beck, Dr. Di Yan, Dr. Hongjun Chen, Prof. Antonio Tricoli, Prof. Kylie Catchpole and Dr. Siva Karuturi
School of Engineering, The Australian National University Canberra, ACT 2601, Australia

Dr. Haobo Li and Prof. Karsten Reuter
Theoretical Chemistry and Catalysis Research Center, Technische Universität München, Lichtenbergstr. 4, 85747 Garching, Germany

Dr. Yuan Wang, Dr. Zhen Su and Prof. Chuan Zhao
School of Chemistry, Faculty of Science, The University of New South Wales, Sydney, NSW 2052 Australia

Dr. Hongjun Chen and Prof. Antonio Tricoli
Nanotechnology Research Laboratory, Faculty of Engineering, University of Sydney, NSW 2006, Australia

Dr. Asim Riaz, Dr. Kaushal Vora and Dr. Siva Karuturi
Department of Electronic Materials Engineering, Research School of Physics, The Australian National University Canberra, ACT 2601, Australia

Prof. Karsten Reuter
Fritz-Haber-Institut der Max-Planck-Gesellschaft, Faradayweg 4-6, 14195 Berlin, Germany

E-mail: haobo.li@tum.de; kylie.catchpole@anu.edu.au; siva.karuturi@anu.edu.au;

Keywords: Electrocatalyst, Ni₃N synthesis, hydrogen evolution, Si photocathode, nitrogen-vacancies, density functional theory

Experimental Methods

Materials: All chemicals were of analytical grade and were used as-purchased without further

purification. Aqueous solutions were prepared using high purity water produced from a Millipore

Milli Q Purification system (resistivity >18 MΩ cm). Conducting FTO glass (purchased from Yingkou Shangneng Photoelectric material Co., Ltd with a sheet resistance of 7-9 Ω/□) was cleaned by sequential ultrasonication in acetone, ethanol, and deionized water for 30 min each.

Preparation of Ni₃N, Ni₃N/Ni and Pt catalysts: Ni_3N and Ni_3N/Ni catalysts were deposited on FTO glass using a magnetron sputtering system (ATC 2400, AJA International Inc.) loaded with a Ni sputter target with a direct current power of 150 W and a chamber pressure of 4.0 mTorr at room temperature. The deposition times were optimized to achieve a target film thickness of ∼210 nm. For the Ni_3N catalyst, the deposition was carried out under a constant flow of Ar and N_2 gases at 20 SCCM each for 1500 s. For the bilayer Ni_3N/Ni, a Ni film (~70 nm) was first deposited under 20 SCCM Ar gas flow for 500 s, followed by Ni_3N (~140 nm) deposition under a constant flow of Ar and N_2 gases at 20 SCCM each for 1000 s. Pt films were deposited by the same sputtering system at 150 W under 100% Ar flow using a Pt sputter target. The pressure during the sputtering process was held constant at 4.0 mTorr. The total deposition time was fixed at 1500 s which results in 90 nm-thick Pt films.

The porous substrates have been cleaned in the sonicator sequentially in acetone, ethanol, and deionized water for 30 minutes. It should be noted that NF needs 10 minutes sonication in the 3.0 M diluted HCl solution.

Fabrication of Si photocathodes: N-type (100) Si wafers of 300 μm thickness with a phosphorus dopant concentration of 5×10^{15} cm^{-3} were used for the fabrication of Si photocathodes. Light harvesting side of the Si photoelectrodes was prepared by texturing with random pyramids by electroless chemical etching in a 45% KOH solution. The textured Si surface was further subjected to boron diffusion (~100 Ω □$^{-1}$) to form a p-n junction, followed by the depositions of a ~10 nm Al_2O_3 using atomic layer deposition and ~65 nm of SiN_x using plasma-enhanced chemical vapour

deposition as passivation and antireflection layers, respectively. Finally, the light harvesting surface was patterned via photolithography and metallized with a grid of 10 μm width lines and 1.3 mm pitch, deposited from thermal evaporation of a Cr (~10 nm)/Pd (~10 nm)/Ag (~100 nm) stack, followed by thickening with Ag electroplating. The back surface of the resulting Si structure was prepared for the HER in direct contact with the electrolyte solution. Microgrooves were formed on the surface by etching in a maskless reactive ion etching system using SF_6/O_2 plasma, followed by wet chemical etching in a HF and HCl containing solution. The structured surface was then subjected to thermal diffusion of $POCl_4$ to obtain a phosphorous dopant concentration of 3×10^{20} cm^{-3}. Si photocathodes were prepared by sputtering either Ni_3N/Ni or Pt as cocatalysts on the phosphorous diffused Si surface adopting the deposition processes as described above. A Ti layer with a thickness of ~30 nm was introduced between Si and catalysts to improve the band energetics and alleviate charge recombination. Cu metal wires were attached to Ag busbar on the light harvesting side using Ag paste, which was then sealed with a quartz sheet using epoxy (Hysol 11C) to protect from corrosion in the electrolyte.

Material Characterizations: SEM characterizations to obtain surface and cross-sectional images of the synthesized samples were carried out using a Helios Nanolab 600 FIB system. Prior to the preparation of cross-sectional lamellas using the FIB system, a layer of Pt was deposited on the samples within system to avoid damage from Ga ion milling. The crystallinity of the samples was examined by XRD measurements on a Bruker system (D Phaser, USA) equipped with Cu Kα radiation with an average wavelength of 1.54059 Å. The typical scan range (2θ) was 10º to 80º collected with a step size of 0.039º s^{-1}. The TEM and HRTEM images were obtained on a JEF2100 (JEOL company) with an acceleration voltage of 200 kV. XPS measurements were performed with Thermo ESCALAB250i. The high-resolution measurements were conducted with 500 μm spot size

and a pass energy of 20 eV. To ensure the consistency of the results, the scan was performed at 4 different spots. The binding energies reported in this study were calibrated to adventitious hydrocarbon at 284.8 eV.

Electrochemical characterizations: Current density vs. potential curves were recorded with a commercial potentiostat (CHI760D electrochemical workstation) in a standard three-electrode configuration, with a Luggin capillary joining the reference electrode (RE) to the working electrode (WE) compartment. A graphite rod and a Ag/AgCl were used as the CE and RE, respectively. The measured current values were converted to current density values by dividing them with the geometric areas of the cathodes after encapsulation. Electrochemical measurements were carried out in 1.0 M KOH aqueous solution. Applied potential was swept from -0.4 to 0.1 V vs. RHE at a scanning rate of 5 mV s^{-1}. All the electrochemical experiments were carried out at room temperature (25 $^\circ$C). The overpotential values for different electrodes were collected at steady-state currents of 10 mA cm^{-2} from chronopotentiometry measurements.

The faradaic efficiency of HER catalyzed by Ni_3N/Ni electrodes was measured in a H-type electrochemical cell with a Nafion membrane separator. Gas samples were collected using an airtight syringe at every 15 min intervals and injected into a gas chromatography (SHIMADZU GC-2030 system, TCD, Argon carrier) for the detection of the generated hydrogen. Before measurement, the reaction system was thoroughly degassed with ultrapure nitrogen to expel the entrapped air. Then, a constant current density of 10 mAcm^{-2} was applied to the electrode and the concentration of hydrogen was analyzed. Calibrations were carried out using a similar setup but with two cleaned Pt foils as working and counter electrodes, respectively. Electrochemical impedance spectroscopy (EIS) was carried out at an overpotential of 50 mV vs. RHE and an AC potential frequency ranging from 100 kHz to 10 mHz. The EIS measurement of zero-gap cells was carried out at a potential of 1.6 V and

an AC frequency ranging from 100 kHz to 100 mHz. The program ZView (Scribner Associates Inc.) was used to fit the obtained data to a corresponding equivalent circuit model.

Photoelectrochemical characterizations: The PEC characterizations including LSV and chronoamperometry were performed using a potentiostat (Autolab PGSTAT302N) in a three-electrode configuration. Ag/AgCl and Pt were used as reference and counter electrodes, respectively, in 1.0 M KOH solution under AM1.5G illumination. The electrode potentials versus Ag/AgCl were converted to RHE potentials according to the Nernst equation. Prior to open-circuit potentials measurements, the photoelectrodes were placed under repeated potential cycling at a scan rate of 20 mV s^{-1} in 1.0 M KOH electrolyte until a stabilized cyclic voltammogram was obtained under illumination. And the electrolyte was deoxygenated by bubbling with ultrahigh purity N_2 for 30 min and maintained under N_2 atmosphere during the measurements with 50 s illumination intervals. The current-voltage results from the LSV measurements were converted to the ABPE values using the previously reported method. The IPCE measurements were taken in a three-electrode configuration as a function of wavelength from 300 to 1200 nm using a 1000 W Xe lamp equipped with gratings to generate a monochromatic beam.

Zero-gap electrolyser measurements: Fumapem FA-3-50 anionic membrane, 5 cm^2 Ni flow field electrode plates and $NiFe_2O_4$ anode were acquired from Dioxide Materials. The Ni_3N/Ni cathodes were prepared on various porous substrates via sputtering technique as described above. The membrane was activated by soaking it for 24 hr in 1.0 M KOH solution prior to use. A 5 x 5 cm^2 membrane was sandwiched between the $NiFe_2O_4$ anode and a cathode along with Teflon gaskets with an opening window of 1 cm^2. 1.0 M KOH electrolyte at 3 ml min^{-1} was fed into the inlets of cathode and anode flow field end plates, while the output was collected into an electrolyte reservoir. A potentiostat (Autolab PGSTAT302N) was used for the electrochemical current-voltage

measurements. The cathode plate and anode plates were connected to the working and counter electrode terminals. The zero-gap electrolyser was kept at 55 °C during the measurements.

DFT calculations: All DFT calculations were performed with the plane wave DFT code QuantumESPRESSO (QE)[1] using the van der Waals-corrected BEEF-vdW exchange correlation function[2] with density and wave function cut-offs of 6000 eV and 600 eV, respectively. Adsorption was modelled at fully optimized symmetric slabs, separated by a vacuum region of at least 20 Å. All the structures were fully relaxed until residual forces fell below 0.03 eV/Å. Reciprocal space sampling was performed with a $(2 \times 2 \times 1)$ k-point mesh. Test calculations with higher wave function cut-offs up to 800 eV and k-point grids up to $(4 \times 4 \times 1)$ indicate the obtained H* adsorption energies to be converged within 0.03 and 0.02 eV, respectively. The Ni_3N_{1-x} material was modelled by a (2×2) unit-cell of the (001) facet of hexagonal Ni_3N[3] with 7 Ni_3N layers, while a (2×2) unit-cell of Ni(111) with 7 Ni layers was used for comparison. Solvation effects were considered within an implicit solvation approach using the Environ module provided with QE.[4] The relative permittivity value of the dielectric layer was set to 78.3 to simulate water.

Adsorption free energy calculations: The adsorption free energies of H* (G_H) at standard conditions are conveniently calculated as $G_H = E_H + ZPE + \int C_p dT - TS$, where E_H is the adsorption energy of H* that additionally includes free energy contributions to the free adsorbate, ZPE is the zero-point energy, $\int C_p dT$ is the enthalpic temperature correction and TS is the entropic correction. E_H is calculated as $E_H = E_{surf+H} - E_{surf} - \mu(H)$, where E_{surf+H} is the DFT total energy of the surface adsorbed with H*, E_{surf} is the energy of the corresponding pristine surface and $\mu(H)$ is the chemical potential of H* referenced to $H_2(g)$. More negative G_H values indicate a stronger binding.

Ab Initio Thermodynamics Approach: The Ni_3N_{1-x} catalysts can have Ni-, N- and NH- terminations at the surface and different N vacancies concentrations. The composition is considered as $Ni_xN_yH_z$. The phase diagrams are calculated by evaluating the surface free energy γ. Within the *ab initio* thermodynamics approach, γ is defined as:

$$\gamma = \frac{1}{2A}\left[G_{surf}(Ni_xN_yH_z) - x\mu_{Ni} - y\mu_N - z\mu_H\right] \quad . \quad (1)$$

$G_{surf}(Ni_xN_yH_z)$ is the Gibbs free energy of the surface candidate structure, described via a symmetric slab model with two equivalent surfaces of surface unit-cell area A and containing x Ni atoms, y N atoms and z H atoms. $\mu_{species}$ indicate the chemical potentials of the respective species.

1) The catalyst was synthesized from Ni and nitrogen gas plasma and with the composition of Ni_xN_y:

$$\mu_{Ni} = E_{bulk}(Ni) \quad . \quad (2)$$

$$\mu_N = \Delta\mu_N + \frac{1}{2}E_{N_2(molecule)} + \frac{1}{2}F_{N_2}^{vib} \quad . \quad (3)$$

2) The HER working condition is in the solution and the catalyst surface can be terminated by NH group with the composition of $Ni_xN_yH_z$, depending on the bias U and pH. μ_N is referenced to N_2:

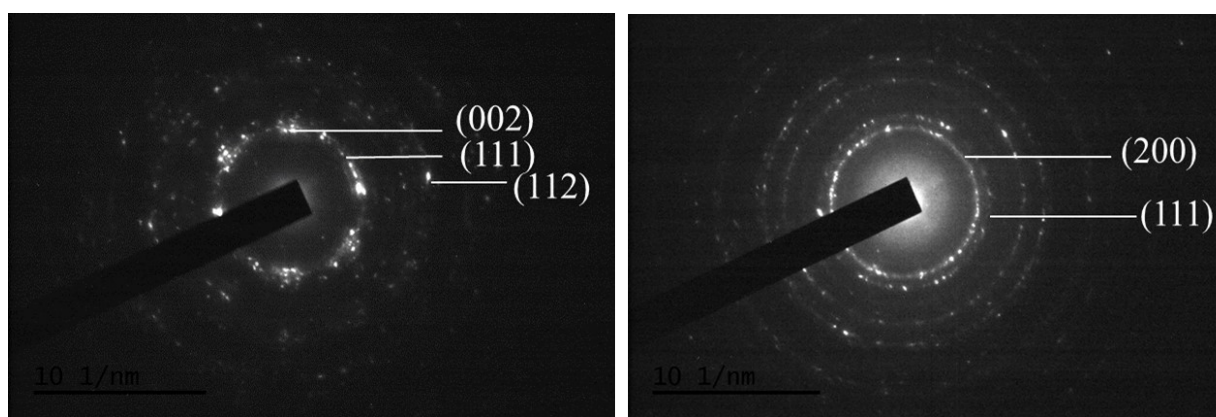$$\mu_N = \frac{1}{2}E_{N_2(molecule)} + \frac{1}{2}F_{N_2}^{vib} + k_BTln(c) \quad . \quad (4)$$

$$\mu_H = \frac{1}{2}E_{H_2(molecule)} + \frac{1}{2}F_{H_2}^{vib} + eU_{SHE} - k_BTlog_{10}(pH) \quad . \quad (5)$$

c is the solubility of N_2 in water at standard conditions. From the approximate N_2 solubility 20 mg/L, c is 1.29×10^{-5} mole fraction.
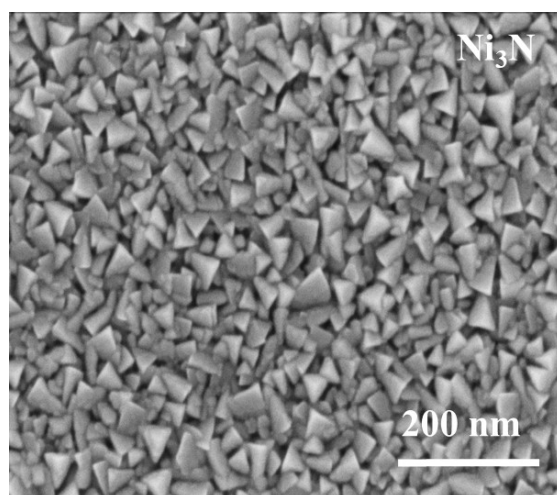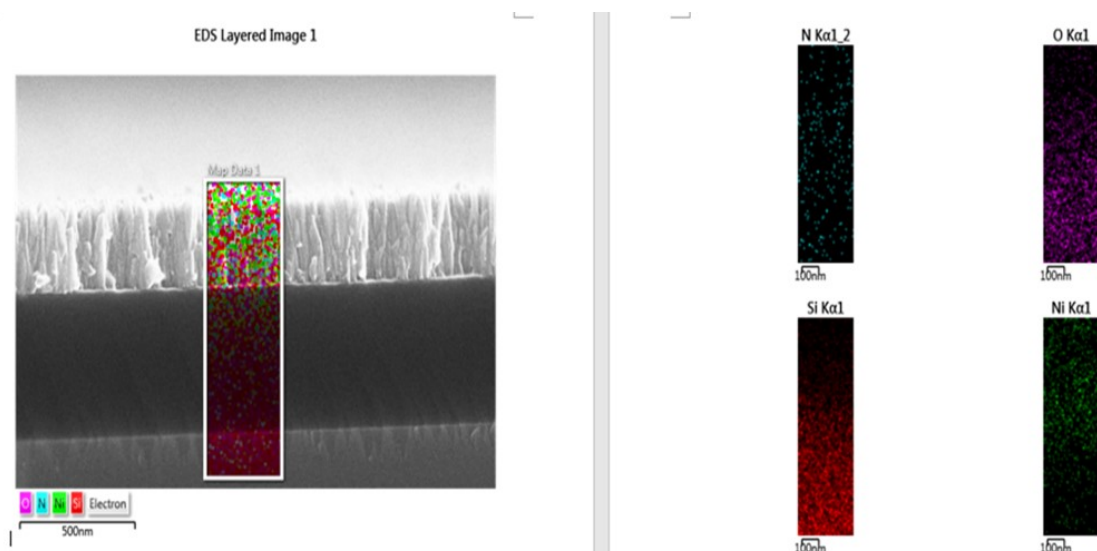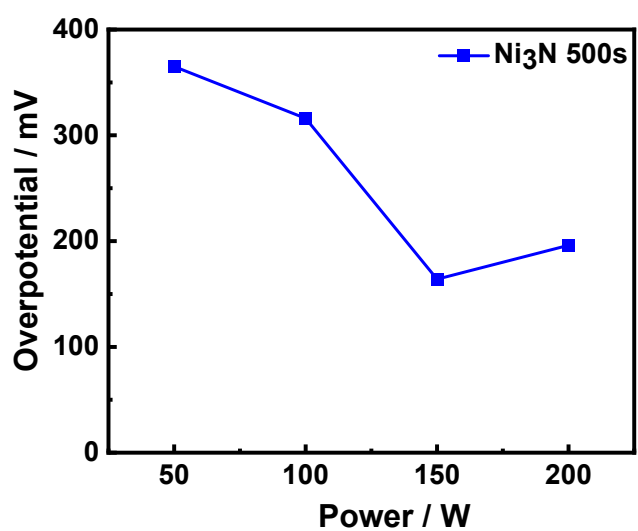
Fig. S1. Scanning electron microscopy image of Ni_3N/Ni on FTO.

Fig. S2. Selected area electron diffraction patterns collected from (a) block 1 (Ni_3N) and (b) block 2 (Ni). Block 1 and 2 are the areas as marked in Fig. 2d in the manuscript.
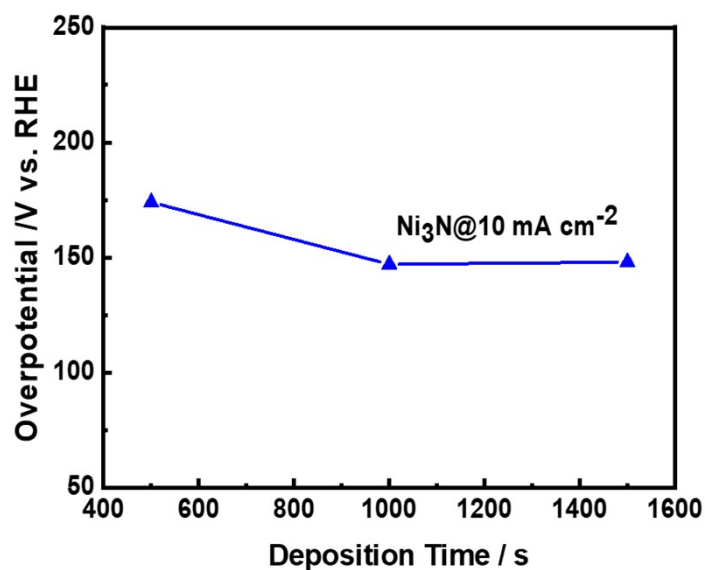
**Fig. S3.** Elemental mapping images obtained from the cross-section of Ni$_3$N/Ni film.

Fig. S4. Overpotential at 10 mA cm^{-2} of Ni$_3$N/FTO electrodes deposited at different sputtering powers for 500 s for the hydrogen evolution reaction in 1.0 M KOH solution.

Fig. S5. Overpotential at 10 mA cm^{-2} of Ni$_3$N/FTO cathodes deposited with different sputtering durations for the hydrogen evolution reaction in 1.0 M KOH solution.
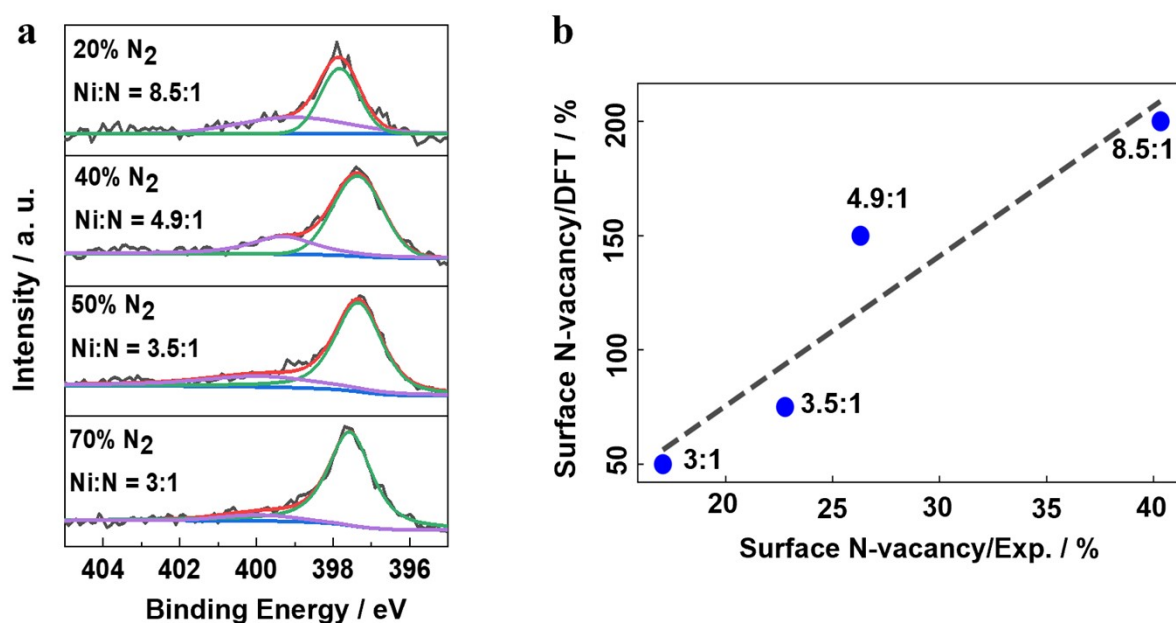
**Fig. S6.** (a) N 1s XPS spectra of a series of Ni$_3$N catalysts sputtered under different N$_2$: Ar ratios. (b) Benchmark of experimental numerical area of N-vacancies in XPS with theoretical N-vacancies used for DFT calculations. The fitted linear relationship between experimental and computational data is shown as black dashed line, with the experimental mixture gas Ni:N ratio given as inset.
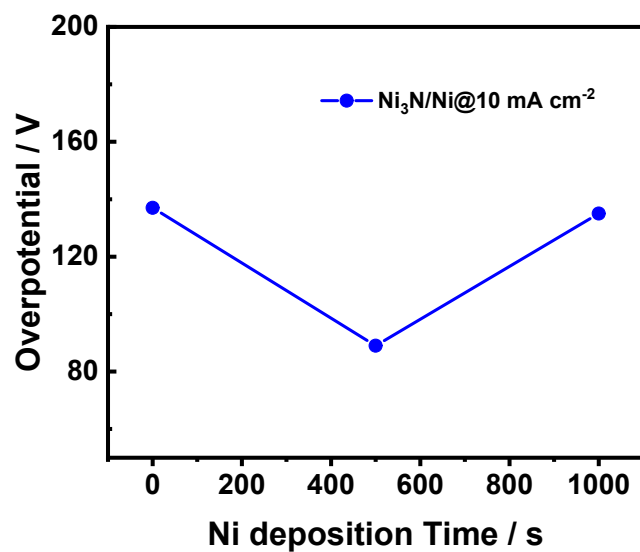
Fig. S7. Overpotential at 10 mA cm^{-2} of Ni$_3$N/Ni/FTO cathodes deposited with different sputtering durations of Ni, followed by sputtering of Ni$_3$N for 1000 s for the hydrogen evolution reaction in 1.0 M KOH solution.
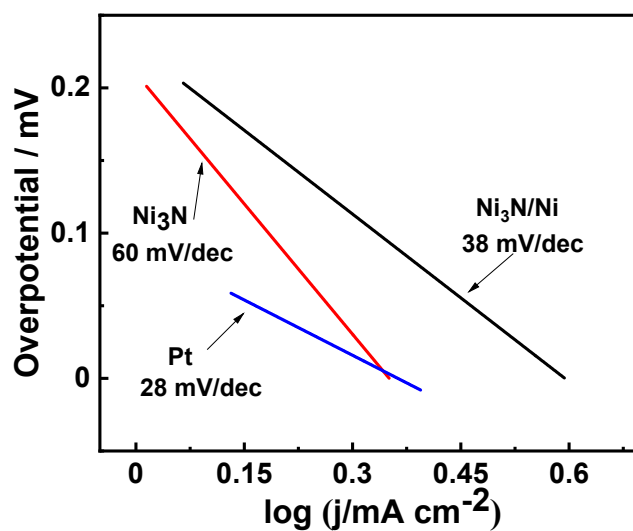
Fig. S8. Tafel plots of Ni$_3$N/Ni/FTO, Ni$_3$N/FTO, and Pt/FTO electrodes derived from their polarization curves presented in Fig. 4b in the manuscript.
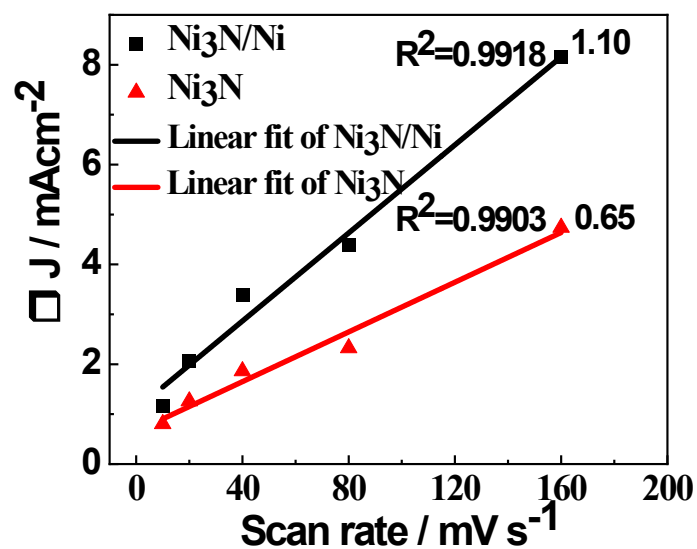
Fig. S9. The linear fittings of the capacitive currents of Ni_3N/Ni and Ni_3N electrodes as a function of scan rate.

**Table S1. The EIS data of different cathodes**

Samples	R_s (Ω cm^2)	CPE-T	CPE-P	R_{ct} (Ω cm^2)
Ni_3N/Ni	9.799	3.7626E-4	1.004	16.19
Ni_3N	9.43	3.0513E-4	0.99521	33.47
Pt	8.252	4.1194E-3	0.6317	3.82

Table S2. Comparison of the HER activity of Ni_3N/Ni on FTO with other earth-abundant electrocatalysts on planar substrates in 1.0 M KOH

| Catalysts	Substrate	Tafel slope (mV/decade)	Overpotential V vs. RHE at -10 mA cm^{-2}	J_0 (mA cm^{-2})	Stability	Reference
Ni_3N/Ni	**FTO**	**38**	**89 (with iR-compensation)**	**0.99**	**75 h**	**This Work**
Ni_3N nanosphere	Ni foil	/	185	/	/	Adv. Energy Mater. 2017, 7, 1601735
$Ni_{11}(HPO_3)_8(OH)_6$	FTO	/	336	/	/	Energy Environ. Sci. 2018,11, 1287-1298
Ni_2P NP	Glass carbon electrode	100	225 (with iR-compensation)	/	48 h	Phys. Chem. Chem. Phys. 2014, 16, 5917-5921
Ni_3FeN	Glassy carbon electrode	42	158	/	9 h	Adv. Energy. Mater. 2016, 6, 1502585
Ni_5P_4 nanosheets	Ni foil	53	150	/	20 h	Angew. Chem. Int. Ed. 2015, 54, 12361
Co-P	Cu foil	42	94 (with iR-compensation)	/	24 h	Angew. Chem. Int. Ed. 2015, 127, 6349-6352
MoC_x	Cu	53	142	0.029	10 h	Nat. Commun. 2015, 6, 6512
Mo_2N	Glassy carbon electrode	108	353	/	1000 cycles	J. Mater. Chem. A 2015, 3, 8361
Mo_2C (10nm)	FTO	78	270	4.4×10^{-3}	10 h (20% degrade)	J. Am. Chem. Soc. 2015, 137, 22, 7035-7038
$TiO_2/Ni/NiMo$	FTO	/	200	/	40 min	J. Mater. Chem. A, 2016, 4, 6842–6852
MoVN	Carbon paper	60	108	/	3000 cycles	Electrochem. Commun. 93 (2018) 166-170
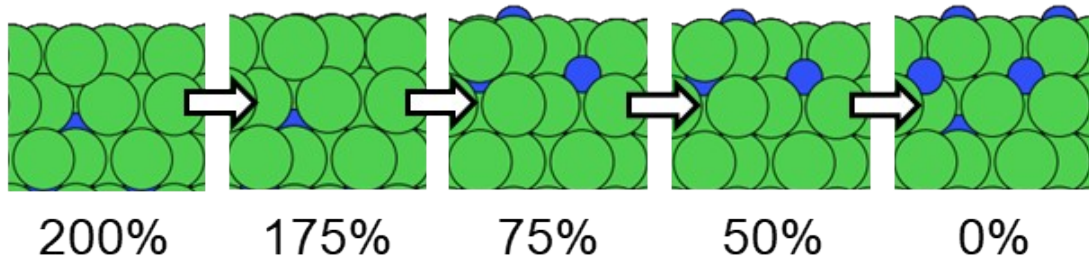
Fig. S10. Atomic structures of Ni_xN_y surface in Fig. 5a with N-vacancies of 200%, 175%, 75%, 50%, 0%, respectively. The perfect Ni_xN_y surface with 0% N-vacancies is formed by alternative N and Ni atomic layers, i.e., "N-Ni-N-Ni-N-Ni…", while a defected surface with 100% N-vacancies corresponds to a fully N-removed surface layer, i.e., "Ni-N-Ni-N-Ni…", and 200% N-vacancies corresponds to first two surface layers which are fully N-removed, i.e., "Ni-Ni-N-Ni-…".
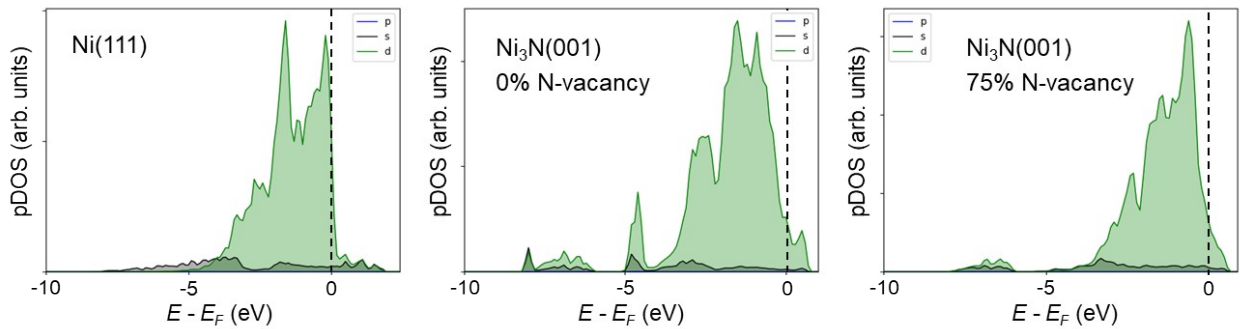

Fig. S11. Projected electronic density of states (pDOS) for surface Ni atoms on Ni(111), $Ni_3N(001)$ with 0% and 75% surface N-vacancies. The Fermi-level is used as zero reference. There is no obvious band gap near the Fermi level, which shows that the three surfaces are all metallic. The corresponding *d*-band center positions are shown in Fig. S12.
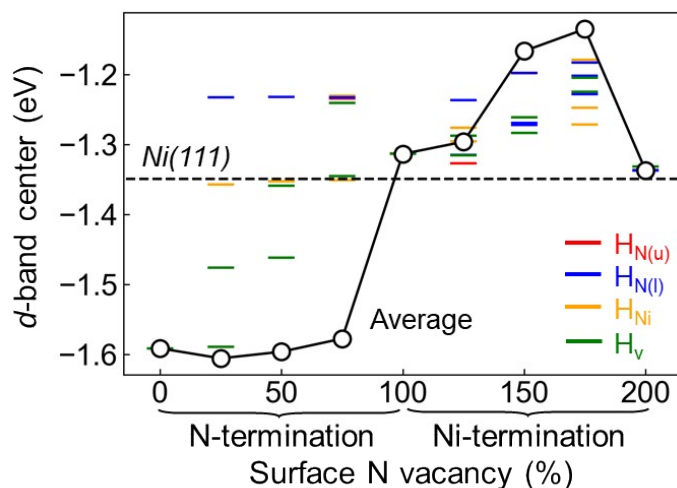
Fig. S12. *d*-band center position (with respect to E_F) of 4 inequivalent Ni$_3$-hollow sites exhibited by a Ni$_3$N(001) surface with varying degree of surface N vacancies. The corresponding values for the Ni$_3$-hollow sites at Ni(111) are shown as dashed line for comparison (the two inequivalent sites share the same value). The average value of the surface Ni atoms for each termination are marked as circles.
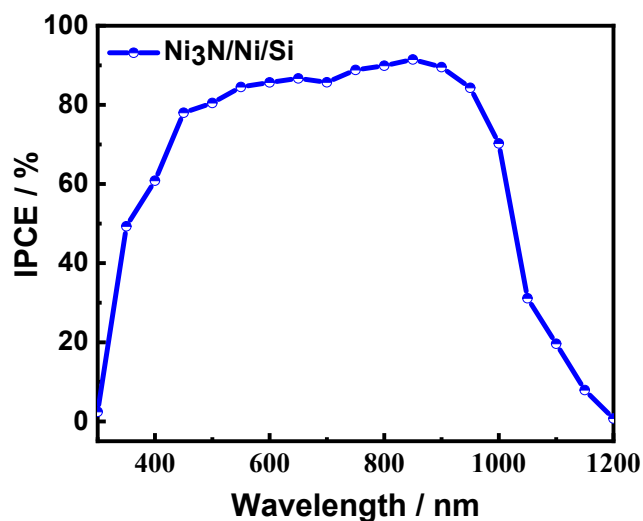
Fig. S13. Incident photon-to-current efficiency of Ni$_3$N/Ni/Si photocathode at 0 V vs RHE. The measurement was performed in 1.0 M KOH electrolyte (pH=14) using a light source equipped with a monochromator.
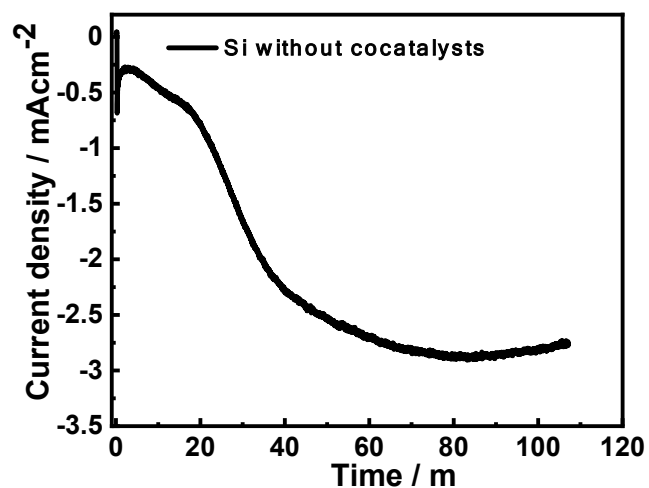
Fig. S14. Chronoamperometry measurements for the Si photocathode without cocatalysts at 0 V vs. RHE in 1.0 M KOH electrolyte under AM1.5 illumination.
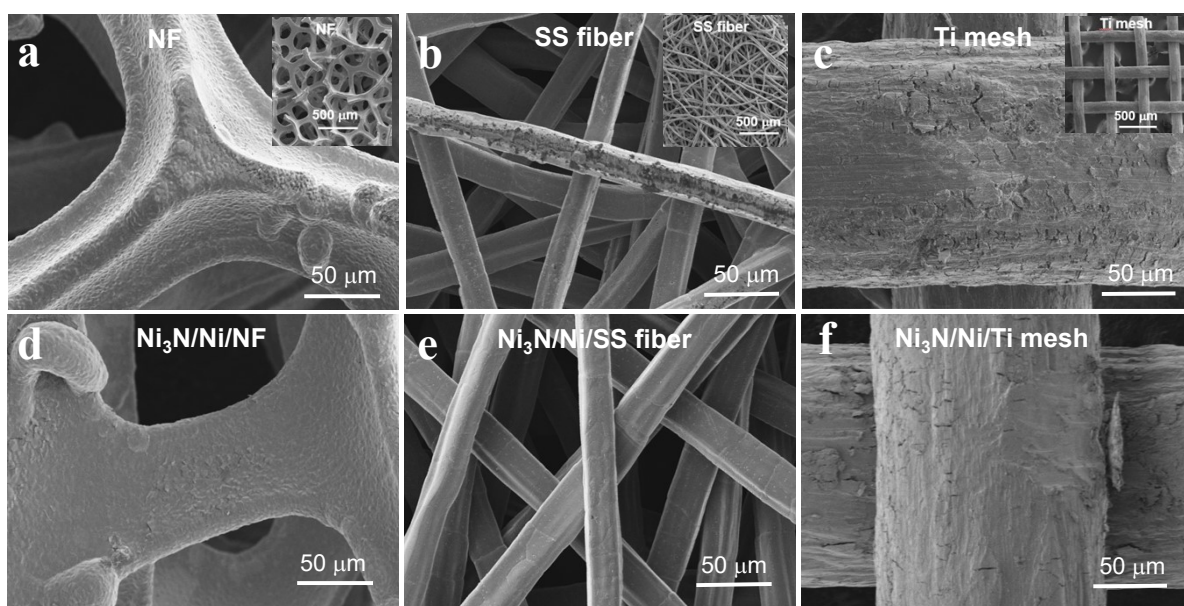

Fig. S15. Scanning electron microscopy (SEM) images of (a-c) blank porous substrates with a scale bar of 50 μm. The insets show low magnification SEM images of the porous substrates with a scale bar of 500 μm. (d-f) SEM images of porous substrates coated with Ni_3N/Ni with a scale bar of 50 μm.

Table S3. The comparison of the performance of Ni-based nitrides on porous substrates in 1.0 M KOH

| Catalyst	Substrate	Fabrication Method	Tafel slope (mV dec^{-1})	Overpotential V vs. RHE at -10 mA cm^{-2}	Stability	Reference
Ni$_3$N/Ni	**Ni foam**	**Magnetron sputtering**	**38**	**66**	**139 h**	**This Work**
Ni$_3$N$_{1-x}$	Ni foam	Microwave plasma	54	55	50 h	Adv. Sci. 2018, 5, 1800406
Ni$_3$N/Ni	Ni foam	Electrodeposition + thermal nitridation	29.3	12	24 h	Nat. Commun. 2018,9, 4531
NiMoN/ Ni$_3$N	Ni foam	Hydrothermal+ thermal treatment	49	28	24 h	Appl. Surf. Sci. 2021, 540, 148407
Cu$_1$Ni$_2$-N	Fiber cloth	Solvothermal+ calcination	106.5	71.4	60 h	Adv. Energy Mater. 2019, 9, 1900390
Ni$_3$N	Ni foam	Calcination	109	121	32 h	Electrochimica Acta.2016, 191, 841–845
MNiNS	Ni foam	Calcination	58.8	119	12 h	J. Mater. Chem. A, 2019, 7, 8117-8121
CoN/Ni$_3$N	Carbon cloth	Hydrothermal +calcination	69	78	24 h	J. Mater. Chem. A, 2018, 6, 4466-4476
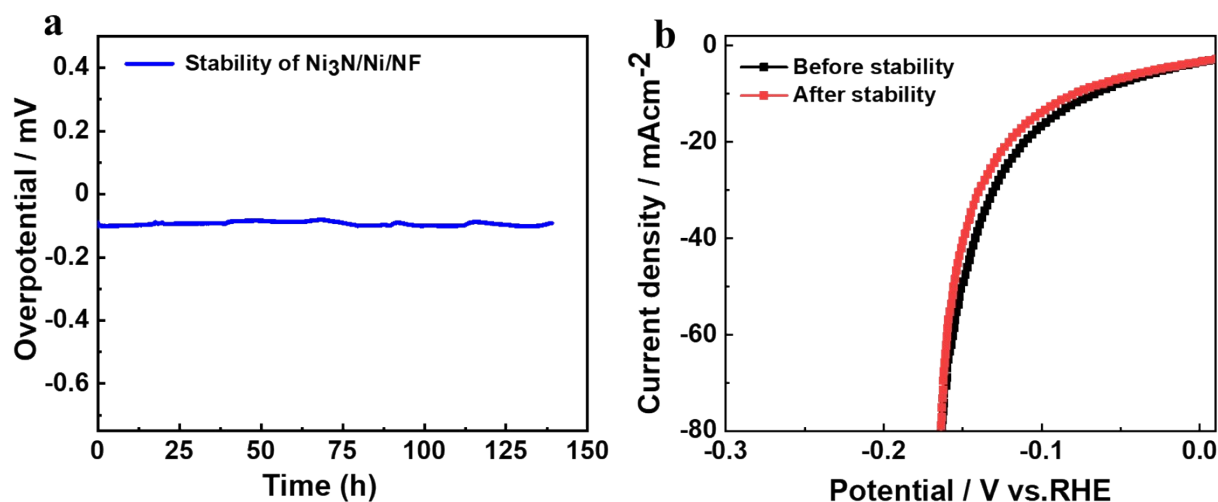
Fig. S16. (a) Chronopotentiometry measurement for Ni$_3$N/Ni/NF electrode at a current density of 15 mA cm^{-2} in 1.0 M KOH in three-electrode configuration. (b) LSV measurements of Ni$_3$N/Ni/NF electrode before and after the stability test.
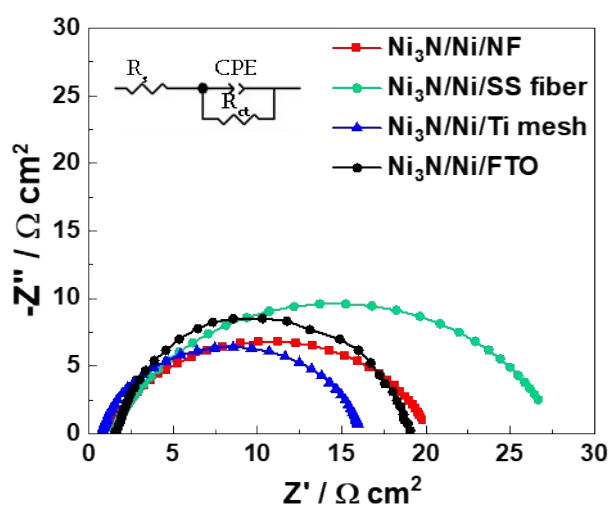

Fig. S17. The Nyquist plots of Ni$_3$N/Ni catalyst on different substrates in three-electrode configuration with Ag/AgCl reference electrode and Pt counter electrode. Electrochemical impedance spectroscopy (EIS) was carried out at an overpotential of 50 mV vs. RHE. The inset shows the Randles circuit. Here, R$_{ct}$ is charge transfer resistance of the electrode, R$_s$ is the series resistance due to wires, contacts, and solution which complete the circuit, and CPE is the constant-phase element which represents the interfacial capacitance.

Table S4. The fitted EIS data of different Ni₃N/Ni coated electrodes

Electrode	R_s (Ω cm^2)	CPE-T	CPE-P	R_{ct} (Ω cm^2)
Ni₃N/Ni/FTO	9.799	3.7626E-4	1.004	16.19
Ni₃N/Ni/NF	1.2266	2.00551E-3	1.031	19.00
Ni₃N/Ni/SS fiber	1.4619	6.31576E-3	0.88504	26.28
Ni₃N/Ni/Ti mesh	0.75121	2.4985E-3	0.70781	15.36
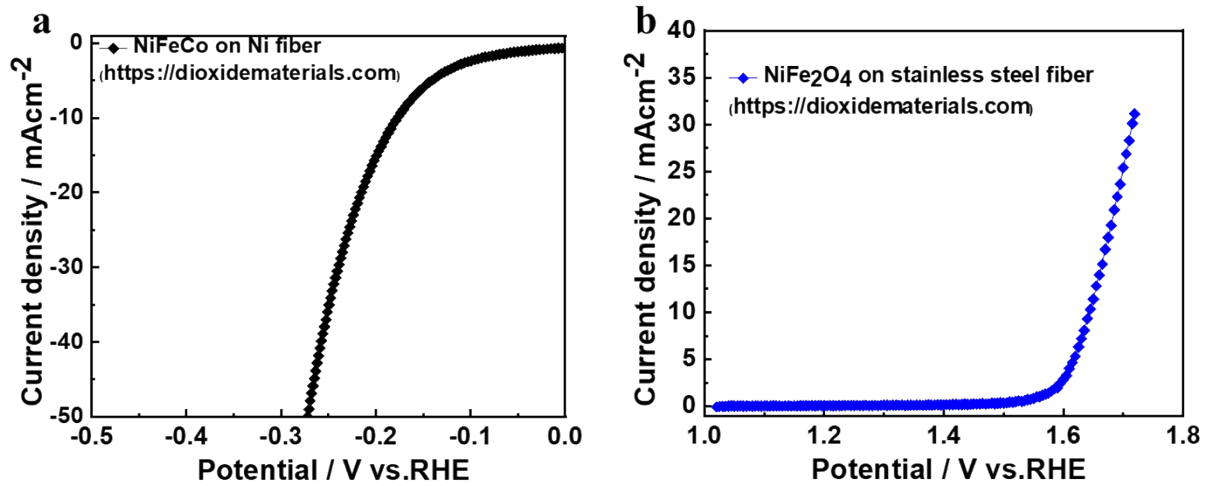
Fig. S18. Linear sweep voltammetry curves (with 90% iR-compensation) of commercial HER and OER electrodes obtained from Dioxide Materials Inc. measured in 1.0 M KOH.
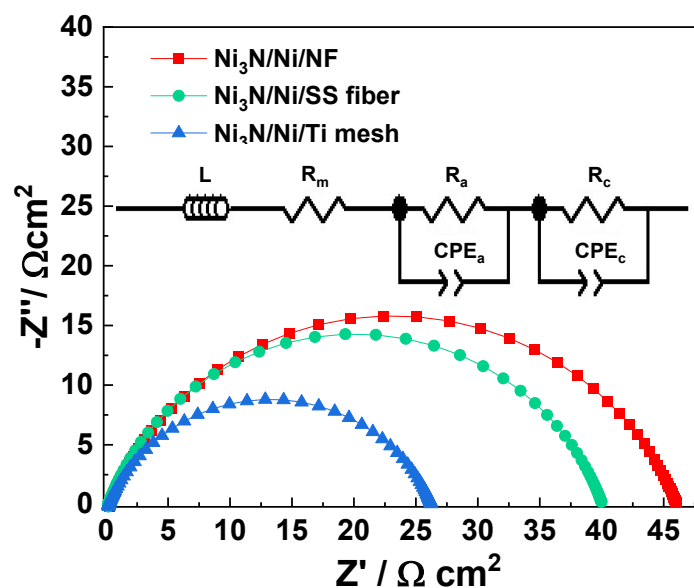
Fig. S19. The Nyquist plots of different porous electrodes in zero-gap cell configuration. The inset is the equivalent circuit model. Here, R_m is membrane resistance, R_a anode resistance, R_c cathode resistance, and CPE_a and CPE_c are constant phase elements of anode and cathode, respectively.

Table S5. The fitted EIS data of different porous electrodes in zero-gap cell

Electrode	R_m (Ωcm^2)	R_a (Ωcm^2)	R_c (Ωcm^2)
$Ni_3N/Ni/NF$	0.22984	0.006	45.82
$Ni_3N/Ni/SS$ fiber	0.16516	0.006	39.88
$Ni_3N/Ni/Ti$ mesh	0.15645	0.006	26.06

Table S6. Performance comparison of Ni-based electrodes in single cell water electrolysis cell at a current density of 0.5 A cm^{-2}

Cathode	Anode	E_{cell} /V	Electrolyte, temperature	References
Ni$_3$N/Ni/Ti mesh	**NiFe$_2$O$_4$/SS fiber**	**1.88**	**1 M KOH, 329.15 K**	**Our work**
NiCoFe/Ni fiber	NiFe$_2$O$_4$/SS fiber	1.86	1 M KOH, 329.15 K	Int. J. Hydrogen Energy, 2017, 42, 29661-29665.
MoNi$_4$/MoO$_2$	NiFe-BTC-GNPs MOF	1.85 (450 mAcm^{-2})	0.1 M KOH, 343.15K	Energy Environ. Sci., 2020, 13, 3447-3458
NiMo-NH$_3$/H$_2$	Fe-NiMo-NH$_3$/H$_2$	1.57 (1 Acm^{-2})	1 M KOH, 353.15 K	Adv. Energy Mater,2020, 10, 2002285
NiFeCo	NiFe$_2$O$_4$	1.9 @1 Acm^{-2}	1 M KOH, 334.15 K	Frontiers in Chemistry. 2018, 263
Uncoactad Ni	NiFe(OH)$_2$	2.23	4 M NaOH, 333 K	Int. J. Hydrogen Energy, 2012, 37, 7429-7435
High area Ni	NiFe(OH)$_2$	2.07	4 M NaOH, 333 K	Int. J. Hydrogen Energy, 2012, 37, 7429-7435
NiAl	NiFe(OH)$_2$	2.06	4 M NaOH, 333 K	Int. J. Hydrogen Energy, 2012, 37, 7429-7435
NiS	NiFe(OH)$_2$	1.95	4 M NaOH, 333 K	Int. J. Hydrogen Energy, 2012, 37, 7429-7435
NiMo	NiFe(OH)$_2$	1.90	4 M NaOH, 333 K	Int. J. Hydrogen Energy, 2012, 37, 7429-7435

References:

1. P. Giannozzi, S. Baroni, N. Bonini, M. Calandra, R. Car, C. Cavazzoni, D. Ceresoli, G. L. Chiarotti, M. Cococcioni and I. Dabo, *Journal of physics: Condensed matter*, 2009, **21**, 395502.
2. C. Guillaume, J. Morniroli, D. Frost and G. Serghiou, *Journal of Physics: Condensed Matter*, 2006, **18**, 8651.
3. J. Wellendorff, K. T. Lundgaard, A. Møgelhøj, V. Petzold, D. D. Landis, J. K. Nørskov, T. Bligaard and K. W. Jacobsen, *Physical Review B*, 2012, **85**, 235149.
4. N. G. Hörmann, Z. Guo, F. Ambrosio, O. Andreussi, A. Pasquarello and N. Marzari, *npj Computational Materials*, 2019, **5**, 1-6.

Author Contributions

D. Zhang: Writing - original draft, data curation, formal analysis. H. Li and K. Reuter: DFT calculation and discussion, and draft review; A. Riaz, A. Sharma, W. Liang, Y. Wang, H. Chen, K. Vora, D. Yan and Z. Su: Data collection, analysis and discussion. A. Tricoli, C. Zhao and F. Beck: Data analysis, and draft review & editing; K. Catchpole: Data analysis, draft review and supervision, and S. Karuturi: Conceptualization, writing - review & editing, supervision.